# Evaluating a Procedure to Align Local Laser Doping and Metallization

Julian Weber, Elmar Lohmüller, Simon Gutscher, and Andreas A. Brand

***Abstract*—We evaluate a procedure that is meant to ensure a highly accurate alignment between laser-doped lines and either screen-printed metal contacts or laser contact openings (LCO) for subsequent galvanic plating of the metal contacts. For both process routes, we prove that the application of the procedure significantly increases the alignment accuracy, discusses potential error sources, and identifies the major challenges for avoiding misalignment. As shown by the presented experiments, the use of screen-printed contacts is challenging for the alignment, since the laser doping process "needs to foresee" the screen print. For plated contacts, however, a much more accurate alignment can be achieved, since the LCO process "can react" on the previously applied laser-doped pattern. As we demonstrate, we are able to combine 10-$\mu$m-wide LCO lines with 36-$\mu$m-wide laser-doped lines (while ensuring that the passivation layer is only opened within the laser-doped area).**

***Index Terms*—Alignment, laser contact opening (LCO), laser-doped selective emitter, screen printing, structuring, silicon solar cells.**

## I. Introduction

THE NEED to align locally applied processes to each other has become a major challenge in solar cell fabrication, since the trend goes to high-efficiency solar cell concepts [1], such as the passivated emitter and rear cell (PERC) with selective emitter [2]–[4], or, e.g., the interdigitated back contact cell [5], [6]. Especially laser-based approaches, such as the laser-doped selective emitter (LDSE) [7]–[9], the PassDop [10]–[12], and the FoilMet-Connect [13] approach, might lead to a boost in solar cell efficiency, but come along with the challenge to align two patterning processes to each other. In this article, a procedure is evaluated that is meant to ensure a highly accurate alignment of two structuring processes to each other. The potential of this alignment procedure has already been demonstrated in [11] and [12], where we last reported on the successful alignment of 40-$\mu$m-wide screen-printed metal contacts to 70-$\mu$m-wide laser-doped lines. In [14], we introduced the alignment procedure by providing detailed insight into its principle. In this article, we point out potential error sources, and we name the key aspects for achieving high alignment accuracies. The focus lies on the LDSE approach for PERC solar cells for which an accurate alignment between the laser-doped lines and the front metal contacts is crucial—not only because misalignment causes large losses in energy conversion efficiency, but also because efficiency is directly increased by reducing the LDSE width [8], [9]. The presented experiments consider the LDSE to be either combined with a screen-printing process for applying the metal contacts or with a laser contact opening (LCO) process followed by galvanic plating of the metal contacts. As we point out, for both process routes, the alignment procedure can be applied to achieve highly accurate alignment.

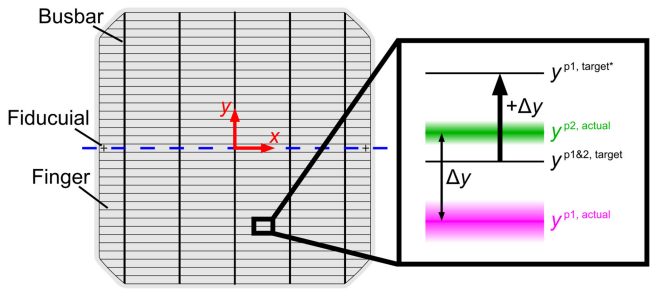


Fig. 1. Solar cell contact grid illustrating the principle of the alignment procedure. The structures of process 1 ("p1") are shifted toward the structures of process 2 ("p2"), in order to match both process patterns. For this, the actual positions $y^{p1,actual}$ and $y^{p2,actual}$ are measured in the coordinate system defined by the fiducials, and subsequently, the target position of process 1 is modified to $y^{p1,target^*}$.

## II. Principle of Alignment Procedure

In this section, we briefly describe the principle of the alignment procedure. For further details, the readers are referred to the extensive introduction of the procedure given in [14]. Fig. 1 illustrates how the principle can be exploited to align two processes (referred to as "process 1" and "process 2"). In this example, process 1 is a laser-doping process forming an LDSE; process 2 is the application of the front metallization grid by screen printing. Both processes not only provide a grid pattern, but also fiducials on the left and right sides of the wafer. Thereby, a unique coordinate system is defined (see left side of Fig. 1), which is referred to as the "fiducial coordinate system" throughout this article. On the right side of Fig. 1, a detailed view on an exemplary spot in the grid pattern (referred to as "grid point") is displayed. Although process 1 and process 2 aim for the same position of the grid point, both the LDSE and the

Manuscript received October 21, 2019; revised December 12, 2019; accepted January 11, 2020. Date of current version February 19, 2020. This work was supported by the German Federal Ministry for Economic Affairs and Energy within the research project "POLDI" under Contract 0324079D. *(Corresponding author: Julian Weber.)*

The authors are with the Fraunhofer Institute for Solar Energy, 79110 Freiburg, Germany (e-mail: julian.weber@ise.fraunhofer.de; elmar.lohmueller@ise.fraunhofer.de; simon.gutscher@ise.fraunhofer.de; andreas.brand@ise.fraunhofer.de).

Color versions of one or more of the figures in this article are available online at https://ieeexplore.ieee.org.

Digital Object Identifier 10.1109/JPHOTOV.2020.2966833

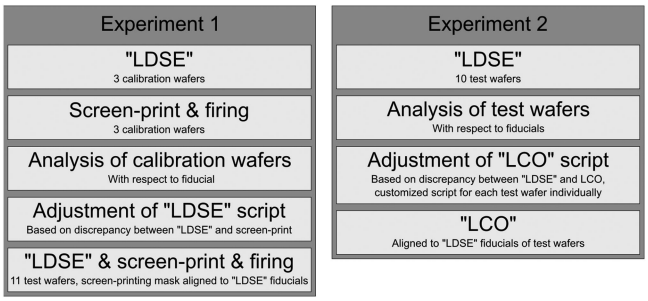


Fig. 2. Flowcharts showing each step of the alignment procedure in experiment 1 (left) and experiment 2 (right). In experiment 1, the "LDSE" is adjusted to a screen-printed grid structure. In experiment 2, an LCO pattern is aligned to the "LDSE."

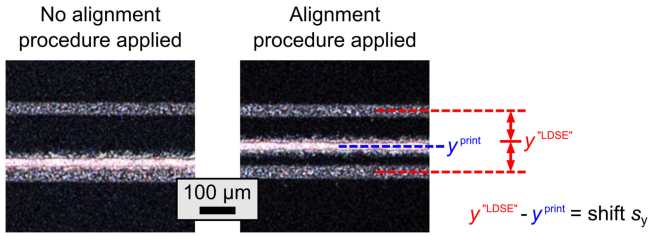


Fig. 3. Exemplary microscope images of a reference wafer (left image) and a test wafer for which the alignment procedure is applied (right image). The alignment procedure aimed for minimizing the shift $s_y = y^{\text{"LDSE"}} - y^{\text{print}}$ between the screen-printed finger and the center of the "LDSE lines." The fingers feature a width of $(38 \pm 2)$ $\mu$m, whereas the width of the "LDSE lines" is $(41 \pm 1)$ $\mu$m.

contact finger might miss the targeted $y$-position $y^{p1\&2,\text{target}}$, if no special alignment procedure is conducted. As the accuracy of the process technologies is not perfect, the $y$-positions $y^{p1,\text{actual}}$ and $y^{p2,\text{actual}}$ might be hit. Note that these positions are not sharply defined, but rather scatter (as the color gradient in Fig. 1 indicates). Also, the reproducibility of the technologies is limited as well. In order to match $y^{p1,\text{actual}}$ and $y^{p2,\text{actual}}$, one of the processes needs to be adjusted with respect to the other one. The screen-printing pattern cannot be economically adapted. As the laser process is the "flexible" one, $y^{p1,\text{actual}}$ is shifted toward $y^{p2,\text{actual}}$. Thus, the target position of the LDSE process is changed from $y^{p1\&2,\text{target}}$ to

$$y^{\text{p1,target}^*} = y^{\text{p1\&2,target}} + \left(y^{\text{p2, actual}} - y^{\text{p1, actual}}\right). \quad (1)$$

When it comes to screen printing, the screen-printing mask is aligned to the laser-processed fiducials in order to match both process patterns.

In short, the key concept of the alignment procedure is to match both process patterns by bringing the fiducials in accordance. As long as LDSE and metallization match, it is irrelevant, whether the targeted design of the grid is realized and whether the grid position/orientation is perfectly aligned to the wafer edges. In other words, the alignment accuracy is independent to the individual accuracies of processes 1 and 2 and to the coordinate system given by the wafer edges.

If galvanic plating is used for metallization of the solar cells instead of screen printing, process 2 will be the LCO process. In this case, it is possible to shift $y^{p2,\text{actual}}$ toward $y^{p1,\text{actual}}$ by setting the target position of the LCO to

$$y^{\text{p2,target}^*} = y^{\text{p1\&2, target}} - \left(y^{\text{p2,actual}} - y^{\text{p1, actual}}\right). \quad (2)$$

Equation (1) and (2) refer only to the $y$-positions. The alignment of the $x$-positions, however, works the same.

## III. Experimental

Two experiments are performed in order to evaluate the alignment procedure; see Fig. 2. In the first experiment, the alignment between LDSE and screen printing is tested; the second experiment deals with the alignment between LDSE and LCO. However, no solar cells are fabricated. Instead, the experiments are performed on test wafers (Czochralski-grown silicon wafers with 156 mm edge length and a silicon nitride passivation layer). Instead of applying an LDSE, each LDSE line is replaced by a pair of laser ablation lines (further referred to as "LDSE lines"). The goal is to apply the alignment procedure such that the screen print/LCO sits exactly in the center between the "LDSE lines"; see Figs. 3 and 6. For characterizing any applied pattern in this article, a coordinate measuring machine is used. The maximal error in accuracy of this system is about 1 $\mu$m. The same holds for the maximal reproducibility error of the system. The accuracy was measured using a calibration plate (glass plate coated with a vapor-deposited metal pattern); the reproducibility is tested by measuring a pattern of laser ablation lines ten times in a row. Due to the high precision of the coordinate measuring machine, measurement errors are neglected in this article.

### A. Aligning LDSE and Screen-Printed Metal Contacts

In the first experiment, the "LDSE lines" (process 1) are adjusted in order to match a screen-printed grid pattern consisting of 110 fingers (process 2). The "LDSE lines" are applied using a laser setup (build for research and development) with a galvanometer scanner system. The wafers are aligned to three metal pins in the laser setup, in order to reproduce their position in the laser scan field. The alignment procedure is conducted as follows (see left side of Fig. 2). At first, three calibration wafers with "LDSE lines" are fabricated using the laser setup in a calibrated state. However, the laser script is manipulated by introducing an artificial offset of 50 $\mu$m in order to "complicate" the alignment. Besides the "LDSE" calibration wafers, three screen-printed and fired calibration wafers are fabricated. In the next step, all six calibration wafers are analyzed by measuring the positions $y^{p1,\text{actual}}$ and $y^{p2,\text{actual}}$ (see Fig. 1) at seven grid points per "LDSE line"/finger. Based on (1), an adjusted "LDSE" script is generated (telling the galvanometer scanner system to connect the seven target positions $y^{p1,\text{target}^*}$ per "LDSE line" without changing the scan speed). Finally, the adjusted "LDSE" process is conducted, the screen print is applied (while aligning the printing mask to the laser-processed fiducials), and contact firing is performed. Besides 11 test wafers that undergo the described alignment procedure, 6 reference wafers are processed without adjusting the "LDSE lines."

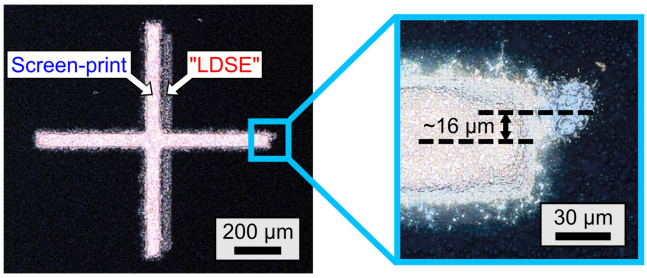


Fig. 4. Exemplary microscope images showing the $y$-shift between the screen-printed fiducial on top of the laser-processed fidcuial. In this example, the $y$-shift is about 16 $\mu$m. The $x$-shift is not of interest.

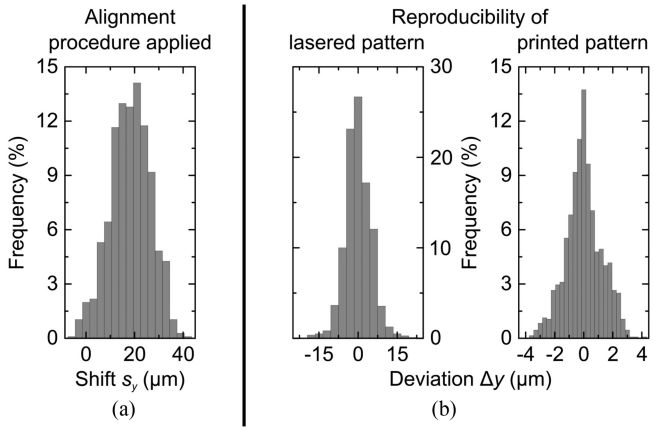


Fig. 5. (a) Histogram of the shift $s_y = y^{\text{"LDSE"}} - y^{\text{print}}$ (see Fig. 2) representing the measurement results for the test wafer group for which the "LDSE" is adjusted to the screen print. (b) Reproducibility of the (left) laser-processed and (right) screen-printed patterns. The graphs result from comparing the process result of multiple wafers (referring to the fiducial coordinate system). The deviation $\Delta y$ represents the scattering of the grid point positions in $y$-direction with respect to the corresponding mean $y$-positions.

### B. Aligning LDSE and LCO

In the second experiment, we pursue a highly accurate alignment between "LDSE" (process 1) and LCO (process 2) by adjusting the LCO. The alignment procedure shown on the right side of Fig. 2 is conducted. First, ten test wafers are fabricated using an (calibrated) industrial laser setup with a galvanometer scanner system. A pattern of 7 × 7 (horizontal and vertical) "LDSE lines" is applied. Next, the "LDSE" positions $x^{p1,\text{actual}}$ and $y^{p1,\text{actual}}$ (see Fig. 1) are measured for all test wafers. Based on these measurements, (2) is applied for generating a customized LCO laser script (with seven grid points per line) for each wafer. In fact, a simplified version of (2) is applied, since the setup used for the LCO—a laser setup with fixed optics build for research and development (referred to as the "LCO laser setup")—is assumed to be perfectly accurate ($x^{p2,\text{actual}} = x^{p1\&2,\text{target}}$, $y^{p2,\text{actual}} = y^{p1\&2,\text{target}}$). Finally, the test wafers receive their individually customized LCO treatment. Besides the ten test wafers, ten reference wafers are processed without any LCO adjustment.

## IV. Results and Error Analysis

### A. Aligning LDSE and Screen-Printed Metal Contacts

Fig. 3 shows exemplary microscope images of one of the reference wafers without correction (left image) and of one of the test wafers for which the alignment procedure is applied (right image). On the reference wafer, the screen-printed finger touches the bottom "LDSE line." This is expected, since the alignment is "complicated" on purpose by introducing an offset of 50 $\mu$m. As we analyze all reference wafers (nearly 100 representative spots per wafer are investigated), we find that with a probability of about 67%, the screen-printed finger is sitting on top of the bottom "LDSE line" (as can be seen on the left side of Fig. 3). For the test wafers, for which the alignment procedure is applied, the finding is different: In 100% of the cases, the screen-printed finger sits in between both "LDSE lines"; see right side of Fig. 3. We conclude that thanks to the alignment procedure, the "LDSE lines" show significantly improved match with the fingers. We, however, expect a systematic offset between the center of the "LDSE lines" $y^{\text{"LDSE"}}$ and the position of the screen print $y^{\text{print}}$, since we find the left fiducials being shifted against each other in $y$-direction by (17 ± 2) $\mu$m; see Fig. 4.

In order to quantify the alignment accuracy achieved by applying the alignment procedure, we measure the shift between the "LDSE lines" and the fingers $s_y = y^{\text{"LDSE"}} - y^{\text{print}}$ at nearly 100 representative positions for each of the 11 test wafers. Fig. 5(a) shows the resulting histogram of $s_y$. By applying a Gaussian fit, $\mu = (19 \pm 0)$ $\mu$m is found to be the center of the $s_y$-distribution. This value is in good accordance with the $y$-shift between the left fiducials of (17 ± 2) $\mu$m; see Fig. 4. We conclude that if the fiducials would have been brought into accordance, the $s_y$-distribution would not have been centered around $\mu \approx 19$ $\mu$m but close to 0. In the following, an extensive further error discussion is presented. In particular, the width of the $s_y$-distribution, which is considered to be six times the standard deviation of the Gaussian fit $6\sigma = (51 \pm 1)$ $\mu$m, shall be associated with potential error sources. In principle, the following error source might have occurred in the presented experiment.

1) The screen-printing mask is not perfectly aligned to the fiducials of the "LDSE" pattern. Therefore, the process patterns are shifted and/or rotated against each other.
2) The number of grid points is not sufficient, which leads to misalignment in between.
3) The "LDSE lines" are linearly shifted toward the expected finger positions. The distortion of the laser scan field, however, is not linear.
4) For processing the calibration wafers, the scanner is fed with a start point and an end point for each line. For processing the test wafers, these two points are replaced by seven grid points per line. Thus, the scanning of the lines is modified.
5) The reproducibility of the processed patterns (with respect to the fiducial coordinate system) is limited.

Error source 1) has already been discussed. It is the only error that can cause a systematic misalignment and is responsible for the $s_y$-distribution being centered on $\mu \approx 19$ $\mu$m instead of 0.

In contrast, error sources 2)–5) cannot be systematic (remember that 770 grid points per wafer are used and $s_y$ is measured at nearly 1100 spots on 11 wafers). Thus, they all contribute to the width of $s_y$. Thereby, error source 5) plays the major role. This is tested with the laser setup processing ten wafers in a row. Besides two fiducials on the wafer edges, a cross pattern of 11 × 11 laser ablation lines is applied. Subsequently, the $y$-positions of the crosses are measured with respect to the fiducial coordinate system. For each cross (for example, cross 1 × 1 at the left bottom corner of the wafers), a mean $y$-position is determined (considering the measurement results of all ten wafers). Finally, the deviations $\Delta y$ between the single measurements and the corresponding mean values are calculated. The left side of Fig. 5(b) shows $\Delta y$ as a histogram summarizing all measurement results obtained in the side experiment. The width of the $\Delta y$-distribution is found to be $6\sigma = (27 \pm 1)\ \mu$m. Note that this value reflects the reproducibility error of the laser-processed pattern with respect to the fiducial coordinate system and not (only) the reproducibility error of the galvanometer scanner system. First, there are further error sources (as, e.g., fluctuation of the wafer position in the laser scan field). Second, not only the laser-processed crosses are subject to the reproducibility error of the galvanometer scanner system, but also the fiducials and thus the fiducial coordinate system and all cross positions in it.

The screen-printed pattern is also investigated regarding reproducibility. The resulting histogram of $\Delta y$ is shown on the right side of Fig. 5(b). It represents the data of 12 wafers that are printed at 3 different sessions (between the sessions, the screen-printing mask was not in use) and analyzed at 110 grid points per wafer. In this case, the $\Delta y$-distribution is $6\sigma = (7 \pm 0)\ \mu$m wide. Thus, the screen-printed pattern shows an increased reproducibility compared with the laser-processed pattern. Note, however, that when printing multiple 1000 wafers in a solar cell fabrication line, the reproducibility might decline due to a warp of the screen-printing mesh. Combining the results obtained in both side experiments, the histogram widths sum up to $6\sigma \approx 34\ \mu$m. Note that this is the width expected for the distribution of $s_y$ in Fig. 5(a), if the only error source present during processing the test wafers is the fluctuation of the screen-printed and laser-processed patterns. The same fluctuations, however, must have occurred during processing the calibration wafers. Thus, the data base for adjusting the "LDSE" is not representative (since only three calibration wafers for each process are analyzed). In consequence, the contribution of error source 5) to the width of the $s_y$-distribution in Fig. 5(a) ($6\sigma \approx 51\ \mu$m) is expected to be even larger than the determined value for $6\sigma \approx 34\ \mu$m.

The presented error analysis let us identify two major requirements for avoiding misalignment between an LDSE and screen-printed metal contacts: a precise match of the fiducials and a high reproducibility of the applied technologies. In this context, we recommend to use not two but multiple fiducials per wafer. This will help to reduce the sensitivity of the fiducial coordinate system to reproducibility errors and to avoid a fiducial mismatch. At the same time, however, this will increase the impact of the other error sources on the alignment accuracy.

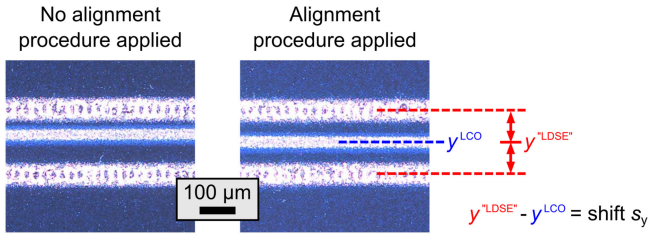


Fig. 6. Exemplary microscope images of a reference wafer (left image) and a test wafer for which the alignment procedure is applied (right image). The alignment procedure aimed for minimizing the shift $s_y = y^{\text{"LDSE"}} - y^{\text{LCO}}$ between the LCO line and the center of the laser ablation lines representing the LDSE. The LCO lines feature a width of $(34 \pm 1)\ \mu$m, whereas the width of the "LDSE lines" is $(65 \pm 2)\ \mu$m.

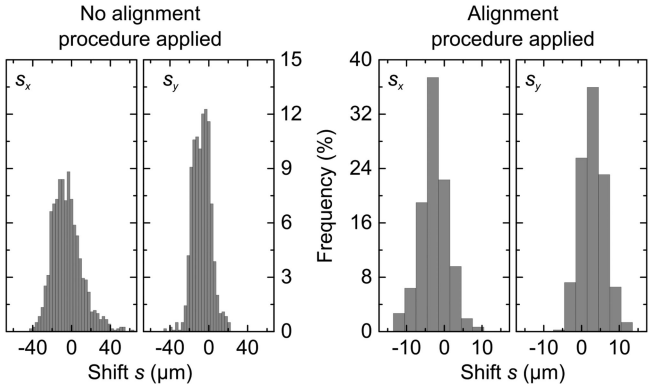


Fig. 7. Histograms of the shifts $s_x = x^{\text{"LDSE"}} - x^{\text{LCO}}$ and $s_y = y^{\text{"LDSE"}} - y^{\text{LCO}}$ (refer to Fig. 5) for the (left) reference wafers and (right) the test wafers for which the LCO was adjusted to the "LDSE."

### *B. Aligning LDSE and LCO*

Fig. 6 shows exemplary microscope images of one of the reference wafers (left image) and of one test wafer for which the alignment procedure is applied (right image). On the reference wafer, the position of the LCO line $y^{\text{LCO}}$ is clearly shifted against the center of the "LDSE lines" $y^{\text{"LDSE"}}$. In the right image, the shift $s_y = y^{\text{"LDSE"}} - y^{\text{LCO}}$ between "LDSE" and LCO is only marginal. In Fig. 7, $s_y$ is shown as histogram. Furthermore, the histogram of the $x$-shift $s_x$ between "LDSE" and LCO is also shown. Each histogram represents nearly 1200 single measurements. On the left side of Fig. 7, the results obtained for the ten reference wafers are presented. The right side corresponds to the ten test wafers for which the LCO is adjusted. By applying Gaussian functions to the plotted distributions, the following conclusions are drawn: With the help of the alignment procedure, the distribution widths could be drastically reduced—for $s_x$ from $6\sigma = (82 \pm 2)\ \mu$m to $6\sigma = (20 \pm 1)\ \mu$m, for $s_y$ from $6\sigma = (57 \pm 2)\ \mu$m to $6\sigma = (20 \pm 0)\ \mu$m. Furthermore, the alignment procedure helped to shift the centers of the distributions toward 0—for $s_x$ from $\mu = (-7 \pm 0)\ \mu$m to $\mu = (-3 \pm 0)$ µm and for $s_y$ from $\mu = (-7 \pm 0)\ \mu$m to $\mu = (3 \pm 0)\ \mu$m. Thus, for the ten test wafers, not only improved but in fact excellent alignment accuracy is achieved.

The test wafers are further analyzed in order to investigate by which error source the alignment accuracy is limited. Remember that applying the alignment procedure involved the generation of an individually customized LCO laser script for each wafer (see Fig. 2). Thereby, the potentially greatest error source—the limited reproducibility of the "LDSE" and the LCO pattern (error source 5) in the first experiment—is eliminated. Since the LCO laser setup is assumed to be perfectly accurate and no calibration wafers are used, the error sources 3) and 4) in the first experiment are eliminated as well. Hence, only the following three error sources might cause the misalignment between "LDSE" and LCO.

1) The LCO pattern is not perfectly aligned to the fiducials of the "LDSE" pattern. Thus, a shift and/or a rotation between the LCO and the "LDSE" is introduced.
2) The number of grid points is not sufficient, which leads to misalignment in between.
3) It is assumed that the LCO laser setup hits the targeted positions given in the LCO laser scripts ($y^{p2,\mathrm{actual}} = y^{p1\&2,\mathrm{target}}$; see Fig. 1). The accuracy of the LCO pattern is, however, limited.

Error sources 1) and 2) are the same as in the first experiment. In this experiment, however, 1) does not lead to a systematic error, since the fiducial detection is conducted manually by the operator of the LCO laser setup and is therefore only subjected to random fluctuations. In order to judge error source 3), the LCO laser setup is used to process ten wafers in a row. Besides two fiducials on the wafer edges, a cross pattern of $11 \times 11$ LCO lines is applied. Subsequently, the $x$- and $y$-positions of the crosses are measured with respect to the fiducial coordinate system and compared with the target positions in the LCO laser script. The deviations between the target and the actual positions are plotted as histogram (not shown). The deviations distribute around $\mu = (0.5 \pm 0.0)\ \mu$m. The width of the distribution is found to be $6\sigma = (11 \pm 0)\ \mu$m. Thus, the LCO laser setup yields indeed a highly accurate placement of the LCO structures. However, the errors caused by 3) can explain more than half of the scattering the $s_x - /s_y$-distributions show on the right side of Fig. 7. In order to gain further insight into the contribution of 1)–3) to the total scattering of $s_x$ and $s_y$, a $y$-scan along with a pair of vertical "LDSE" lines (with LCO in between) is recorded using the coordinate measuring machine; see Fig. 8. The measurement shows the center position between the "LDSE lines" $x^{\text{"LDSE"}}$ and the LCO position $x^{\mathrm{LCO}}$ (refer to Fig. 6), which we track while moving from the bottom to the top of the wafer. The positions are recorded with respect to the fiducial coordinate system. Subsequently, the coordinate origin is redefined to simplify the presentation of the measurement results. When judging Fig. 8, remember that for each LCO line, seven grid points are used at which the target positions in the LCO laser script are set to $x^{\text{"LDSE"}}$. Between these grid points, a straight connection is expected, since the LCO lines should, in ideal case, directly connect the grid points with each other. Thus, the LCO position $x^{\mathrm{LCO}}$ should ideally match the black line shown in Fig. 8. Indeed, the LCO position $x^{\mathrm{LCO}}$ almost perfectly follows the course of the interpolation—although the distortion of the galvanometer scanner system let the "LDSE" lines scatter in a range of $-15\ \mu\mathrm{m} \leq x^{\text{"LDSE"}} \leq 11\ \mu\mathrm{m}$.

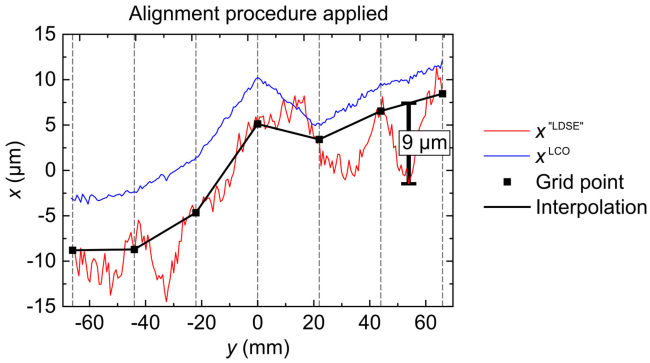


Fig. 8. $y$-Scan along a pair of "LDSE lines" with LCO in between (recorded with the coordinate measuring machine). The measurement shows the LCO position $x^{\mathrm{LCO}}$ and the center position between the "LDSE lines" $x^{\text{"LDSE"}}$ (refer to Fig. 5) across the wafer. For applying the LCO, seven grid points are used at which the target positions in the LCO laser script are set to $x^{\text{"LDSE"}}$. Between these grid points, a straight connection is expected, since the LCO lines should in ideal case directly connect the grid points with each other.

However, $x^{\mathrm{LCO}}$ is systematically shifted by $s_x = x^{\text{"LDSE"}} - x^{\mathrm{LCO}} \approx 5\mu$m with respect to the black line. We conclude that the LCO is, in principle, successfully adjusted to the "LDSE." However, the fiducials are not detected perfectly (error 1). The slight fluctuations $s_x = x^{\text{"LDSE"}} - x^{\mathrm{LCO}}$ along the $y$-direction can be associated with error source 3). We further conclude from Fig. 8 that the misalignment occurring between the grid points (error 2) can reach up to $s_x = 9\ \mu$m (as marked on the right edge of the graph). Thus, all three errors 1)–3) play a role in the presented experiment. They are estimated to contribute almost equally to the width of the $\mathrm{s_x} - /s_y$-distribution on the right side of Fig. 7. Note, however, that if the detection of the fiducials had been more precise in the presented experiment (e.g., by using an automatic image processing algorithm), and if further, a larger number of grid points had been used, practically all error sources would have been eliminated, except for the accuracy error of the LCO laser setup of $\pm 6\ \mu$m. This means that, in principle, we could combine a 10-$\mu$m-wide LCO with a 22-$\mu$m-wide laser-doped line (while ensuring that the passivation layer is only opened in the laser-doped area)—despite how poor the accuracy and reproducibility of the laser doping process is.

## V. Discussion

From the extensive error analysis presented in the previous section, we derive the following guidance for achieving a fast and precise alignment (note that the guidance applies to both solar cell research and solar cell mass production).

1) First, it is to clarify which process is aligned to the other one. If process 2 cannot be adapted, process 1 needs to "foresee" the positioning of the structures applied by process 2. This implies that the alignment accuracy is largely depending on the reproducibility errors of both processes and thus makes it essential to use stable systems for processing. If process 2 can be adapted, the situation is different, since process 2 can "react" on the pattern applied by process 1 for each wafer individually. This yields an

intrinsic advantage to the alignment accuracy, since the alignment accuracy is no longer affected by accuracy and reproducibility of process 1, and, thus, only for process 2, a high reproducibility is required. In the ideal case, process 2 is not only adjustable and highly reproducible but also highly accurate. In this case, process 2 can be considered to hit the structures applied by process 1 by simply targeting for them. This means that no calibration wafers are needed.

2) Second, it is to ensure that the applied structures are examined as fast and precise as possible. This might be challenging in some cases, for example, if laser-processed lines are covered by an antireflection coating layer. This challenge could, however, be overcome by using a high-resolution camera and a fast image processing algorithm for making the laser lines visible and detecting them.
3) Finally, it is to eliminate those error sources that can be easily tackled. This involves, in particular, a precise and robust matching of the fiducials, the usage of a large number of grid points, and also calibration wafers (if needed).

## VI. Summary and Conclusion

In this article, we evaluate a procedure that is meant to ensure a highly accurate alignment between two structuring processes. We test the procedure by simulating laser-doped lines (using laser ablation) and combining them with either screen-printed metal contacts or LCO. In both cases, the alignment procedure helps to reduce misalignment. For the screen-printed contacts, misalignment is reduced to (19 $\pm$ 26) $\mu$m. For the LCO, misalignment is only (3 $\pm$ 10) $\mu$m. Such excellent alignment accuracy allows combining 10-$\mu$m-wide LCO lines with 36-$\mu$m-wide laser-doped lines (while the passivation layer remains unopened outside the laser-doped area). Based on the extensive error analysis presented in this article, we give detailed guidance to improve the alignment accuracy. The most essential requirements for avoiding misalignment are the usage of highly reproducible process technologies as well as a perfect match of the fiducials (reference points used to bring the coordinate systems of the process patterns in accordance).

## References

[1] International Technology Roadmap for Photovoltaic, "International Technology Roadmap for Photovoltaic (ITRPV)—2018 results - 10th edition," March 2019. [Online]. Available: https://itrpv.vdma.org/download
[2] A. W. Blakers, A. Wang, A. M. Milne, J. Zhao, and M. A. Green, "22.8% efficient silicon solar cell," *Appl. Phys. Lett.*, vol. 55, pp. 1363–1365, 1989.
[3] M. A. Green, "The passivated emitter and rear cell (PERC): From conception to mass production," *Sol. Energy Mater. Sol. Cells*, vol. 143, pp. 190–197, 2015.
[4] S. Werner *et al.*, "Key aspects for fabrication of P-type Cz-Si PERC solar cells exceeding 22% conversion efficiency," in *Proc. 33rd Eur. Photovolt. Sol. Energy Conf. Exhib.*, 2017, pp. 406–412.
[5] R. J. Schwartz and M. D. Lammert, "Silicon solar cells for high concentration applications," in *Proc. Int. Electron Devices Meeting*, 1975, pp. 350–352.
[6] M. Ernst *et al.*, "Fabrication of a 22.8% efficient back contact solar cell with localized laser-doping," *Phys. Status Solidi A*, vol. 214, pp. 1700318–1700322, 2017.
[7] L. Ventura, A. Slaoui, and J. C. Muller, "Realization of selective emitters by rapid thermal and laser assisted techniques," in *Proc. 13th Eur. Photovolt. Sol. Energy Conf. Exhib.*, 1995, pp. 1578–1581.
[8] U. Jäger, *Selektive Laserdiffusion Für Hocheffiziente Solarzellen Aus Kristallinem Silicium*. München, Germany: Verlag Dr. Hut, 2013.
[9] J. Weber *et al.*, "Simulations on laser-phosphorous-doped selective emitters," in *Proc. 7th World Conf. Photovolt. Energy Convers.*, 2018, pp. 3588–3592.
[10] U. Jäger *et al.*, "Industrial N-type PERL cells with screen printed front side electrodes approaching 21% efficiency," in *Proc. 31st Eur. Photovolt. Sol. Energy Conf. Exhib.*, 2015, pp. 390–393.
[11] E. Lohmüller *et al.*, "Bifacial P-type silicon PERL solar cell with screen-printed pure silver metallization and 89% bifaciality," in *Proc. 33rd Eur. Photovolt. Sol. Energy Conf. Exhib.*, 2017, pp. 418–423.
[12] E. Lohmüller *et al.*, "Towards 90% bifaciality for p-Type Cz-Si solar cells by adaption of industrial perc processes," in *Proc. 7th World Conf. Photovolt. Energy Convers.*, 2018, pp. 3727–3731.
[13] J. Paschen *et al.*, "Folmet-Connect: A new rear metallization upgrade for PERC and other cell concepts," *AIP Conf. Proc.*, vol. 2156, 2019, Art. no. 020004.
[14] E. Lohmüller *et al.*, "High-precision alignment procedures of patterning processes in solar cell production," in *Proc. Prog. Photovolt., Res. Appl.*, 2019, pp. 1–11.